

Alloying of Alkali Metals with Tellurene

Rishabh Jain

Rensselaer Polytechnic Institute

Yifei Yuan

University of Illinois at Chicago

Yashpal Singh

Lawrence Berkeley National Laboratory <https://orcid.org/0000-0003-0431-1079>

Swastik Basu

Rensselaer Polytechnic Institute

Dawei Wang

Xi'an Jiaotong University

Aijun Yang

Xi'an Jiaotong University

Xiaohua Wang

Xi'an Jiaotong University

Mingzhe Rong

Xi'an Jiaotong University

Ho Jin Lee

National Creative Research Initiative Center for Multi-Dimensional Directed Nanoscale Assembly,
Department of Materials Science and Engineering, KAIST, Daejeon 34141,

David Frey

Rensselaer Polytechnic Institute

Rajan Khadka

Rensselaer Polytechnic Institute

Prateek Hundekar

Rensselaer Polytechnic Institute

Sang Ouk Kim

Korea Advanced Institute of Science and Technology

Fudong Han

Rensselaer Polytechnic Institute <https://orcid.org/0000-0003-2507-4340>

Lin-wang Wang

Lawrence Berkeley National Laboratory <https://orcid.org/0000-0001-7061-2692>

David Mitlin

The University of Texas at Austin

Reza Shahbazian-Yassar

University of Illinois at Chicago <https://orcid.org/0000-0002-7744-4780>

Nikhil Koratkar (✉ koratn@rpi.edu)

Rensselaer Polytechnic Institute

Article

Keywords: Tellurene, alkali metals, electrodes, electrochemical performance

Posted Date: August 1st, 2020

DOI: <https://doi.org/10.21203/rs.3.rs-47288/v1>

License: © ⓘ This work is licensed under a Creative Commons Attribution 4.0 International License.

[Read Full License](#)

Alloying of Alkali Metals with Tellurene

Rishabh Jain,^{1} Yifei Yuan,^{2*} Yashpal Singh,³ Swastik Basu,⁴ Dawei Wang,⁵ Aijun Yang,⁵
Xiaohua Wang,⁵ Mingzhe Rong,⁵ Ho Jin Lee,⁶ David Frey,⁷ Rajan Khadka,⁸
Prateek Hundekar,¹ Sang Ouk Kim,⁶ Fudong Han,¹ Lin-Wang Wang,³ David Mitlin,⁴
Reza Shahbazian-Yassar,² and Nikhil Koratkar^{1,8**}*

¹Department of Mechanical, Aerospace and Nuclear Engineering, Rensselaer Polytechnic Institute, 110 8th Street, Troy, NY, 12180, USA.

²Department of Mechanical and Industrial Engineering, the University of Illinois at Chicago, Chicago, Illinois 60607, USA.

³Material Science Division, Lawrence Berkeley National Laboratory, Berkeley, CA, 94720, USA.

⁴Mechanical Engineering Department, University of Texas, Austin, TX, 78712, USA.

⁵State Key Laboratory of Electrical Insulation and Power Equipment, Xi'an Jiaotong University, No 28 Xianning West Road, Xi'an, China.

⁶National Creative Research Initiative (CRI) Center for Multi-dimensional Directed Nanoscale Assembly, Department of Materials Science and Engineering, KAIST, Daejeon 34141, Republic of Korea.

⁷Center for Materials, Devices, and Integrated Systems, Rensselaer Polytechnic Institute, 110 8th Street, Troy, NY, 12180, USA.

⁸Department of Materials Science and Engineering, Rensselaer Polytechnic Institute, 110 8th Street, Troy, NY, 12180, USA

*Equal contribution

**Corresponding author (Email: koratn@rpi.edu)

ABSTRACT

Graphite is ubiquitous as the anode material in lithium-ion batteries, but offers relatively low volumetric capacity (330 to 430 mAh cm⁻³). By contrast, Tellurene (Te) is expected to alloy with alkali metals with high volumetric capacity (~2620 mAh cm⁻³), but to date there is no detailed study on its alloying behavior. In this work, we have investigated the alloying response of a range of alkali metals (A = Li, Na or K) with few-layer Te. In-situ transmission electron microscopy and density functional theory both indicate that Te alloys with alkali metals forming A₂Te. However, the crystalline order of alloyed products varied significantly from single-crystal (for Li₂Te) to polycrystalline (for Na₂Te and K₂Te). It is well established that typical alloying materials (e.g., silicon, tin, black phosphorous) lose their crystallinity when reacted with Li. The ability of Te to retain its crystallinity is therefore surprising. Nudged elastic band calculations and ab-initio molecular dynamics simulations reveal that compared to Na or K, the migration of Li is highly “isotropic” in Te, enabling its crystallinity to be preserved. Such isotropic Li transport is made possible by Te’s peculiar structure comprised of chiral chains bound by van der Waals forces. To evaluate the electrochemical performance of Te, we tested Te electrodes in half-cells vs Li/Na/K metal. While alloying with Na and K showed poor performance, with Li, the Te electrode exhibited a volumetric capacity of ~700 mAh cm⁻³, which is about two-times the practical capacity of commercial graphite. Such Te based batteries could play an important role in applications where high volumetric energy and power density are of paramount importance.

Introduction

Modern human society cannot flourish without an efficient, affordable and safe means for energy storage. Presently, Lithium (Li) –ion batteries (LIBs) are dominating the energy storage landscape from portable electronics and grid storage to the rapidly expanding electric vehicles market^{1,2,3,4,5,6}. As the range of applications of LIBs expand, it is becoming increasingly clear that the traditional LIB chemistry (i.e., the graphite anode and transition metal oxide cathode) is not well-suited in many situations^{7,8,9,10}. One such scenario, is for applications where packing the maximum amount of energy into a limited volume (compact space) becomes critical^{11,12,13,14}. Commercial graphite anodes in particular, have a limited practical volumetric capacity¹⁵ (about 330 to 430 mAh cm⁻³), which restricts the overall volumetric energy density of the LIB device.

One way to address the above issue, is to replace graphite with a higher volumetric capacity material. Tellurium is one such material that is expected to alloy with Li delivering a theoretical capacity of ~2620 mAh cm⁻³. However, bulk tellurium has poor electrical and ionic conductivity and thus cannot be deployed in LIBs. To circumvent this, tellurium-based nanostructures have been synthesized using several methods, which typically lead to the formation of 1-D tellurium structures (such as nanowires or nanotubes) due to the anisotropic structure of bulk tellurium¹⁶. However, recently a controllable hydrothermal method has been developed that can lead to the formation of 2-D Tellurium or Tellurene (Te)^{17,18}. Te has many attractive features when compared to other materials in the 2D family¹⁶. For example, unlike 2-D transition metal dichalcogenides and hexagonal boron nitride, Te displays fast charge carrier mobility (~10³ cm² V⁻¹ s⁻¹)^{19,20}. Further, unlike phosphorene and silicene which are easily oxidized, Te is stable under ambient conditions^{21,22,23,24}. Importantly, few-layered Te can be synthesized using the hydrothermal method with controllable thickness and with a high yield of ~98%¹⁶. All of these attributes, render Te a promising anode material for LIB applications. In spite of this, there is no study to date that has reported the alloying behavior of Te with Li.

In this work, we have investigated how Te reacts with a range of alkali metals including Li, Sodium (Na) and Potassium (K). In-situ transmission electron microscopy (TEM) and density functional theory (DFT) calculations indicate that few-layer Te reacts with alkali atoms (A = Li, Na, and K) to form the alloy phase (Li₂Te, Na₂Te, and K₂Te). Surprisingly, a single-crystal Li₂Te alloying product was obtained, which is very rare during alloy formation^{25,26}, in comparison with polycrystalline Na₂Te and K₂Te. Nudged elastic band (NEB) calculations predict significantly lower barrier energy for Li migration in Te (~0.13 eV) compared with Na migration (~0.32 eV) and K migration (~0.62). NEB further reveals equal barrier energy for Li migration in both “across-belt” and “along-belt” directions in the Te lattice, which is not the case for Na or K migration. Further, Ab-initio molecular dynamics indicates nearly equal mean square displacement of Li along the across and along belt directions, confirming isotropic movement of Li atom in the interior of the few-layer Te. Such isotropic transport was not observed for either Na or K atoms. This explains why the single-crystal Te (obtained following hydrothermal synthesis) maintains its crystalline identity when reacted with Li, but fails to do so when alloyed with Na or K. The preservation of single-crystal structure during lithiation provides a flatter potential profile, which is helpful for practical application, and more importantly, it also helps to eliminate cell degradations related to secondary grains or particles such as micro-cracks, as has been well documented in single-crystal layered transition-metal oxide cathodes²⁷.

To demonstrate feasibility in a battery setting, we assembled and tested half cells of Te vs Li/Na/K metal. Due to high volume expansion during alloy formation with Li (~170%), Na (~280%) and K (~420%), significant capacity fade was observed, especially for Na and K. In the case of Li, the capacity also reduces but stabilizes at ~700 mAh cm⁻³, which is about two-times that of commercial (battery-grade) graphite¹⁵. We show that the capacity fade can be mitigated in a Te/graphene composite electrodes by using graphene as a buffer layer to suppress the pulverization of Te. These results demonstrate that Te can be a promising anode material for LIB applications, especially in situations where high volumetric performance is desired. Our study also provides new fundamental insight as to why certain alloying materials are able to preserve their crystallinity when deployed in batteries.

Results

Synthesis of Tellurene

Experimental methods for the synthesis of 1-D tellurium have been well researched and are categorized into either vapor phase or solution phase processes^{28–29}. Conversely, the synthesis of 2-D tellurium (Te) is not well established. Prior works showed growth of Te on various substrates such as mica³⁰, highly orientated graphite³¹, and graphene/SiC substrates³² using van der Waals epitaxy method. The conventional liquid phase exfoliation method has also been employed for the synthesis of Te³¹. However, such methods face critical challenges in terms of scalability, control over thickness, substrate-free growth, and sensitivity to growth conditions which inhibits its application, especially for energy storage where scalable manufacturing is essential¹⁶. The recently discovered, hydrothermal method^{17,18} can overcome these limitations, and was therefore used in this study for synthesis of Te (grey colored powder, inset of **figure S1a**) (details regarding the growth mechanism and procedures are provided in Methods).

Scanning electron microscopy (SEM) and transmission electron microscopy (TEM) confirmed the presence of a 2-D sheet-like structure with lateral dimensions ranging from 10–30 μm (**figure S1a, c**). Selected area diffraction pattern (SAED) further confirms the high crystallinity of as-synthesized Te (**figure S1d**). The thickness of Te was ~10–20 nm, obtained using atomic force microscopy (AFM), confirming that the Te was few-layered (**figure S1b**). Raman spectroscopy of as-synthesized Te shows three active modes: E₁ mode (~90.8 cm⁻¹), A₁ mode (~120.3 cm⁻¹), and E₂ mode (~140.7 cm⁻¹) (**figure S1e**) which is consistent with the literature¹⁷. Chemical composition of as-synthesized Te was obtained using X-ray photoelectron spectroscopy (XPS). De-convoluted XPS analysis of Te 3d showed the presence of two major peaks at ~571.39 eV and ~581.86 eV which are attributed to 3d_{5/2} and 3d_{3/2} spin-orbital doublets of Te-Te bond, respectively (**figure S1f**). Two small peaks appearing at ~574.73 eV and ~585 eV are attributed to the Te-O bond (slight oxidation of Te is inevitable during the hydrothermal process). X-ray diffraction (XRD) further confirmed the presence of highly crystalline Te, which is also consistent with previous studies (**figure S1g**). It should be noted that three possible phases of Te have been reported theoretically; α-Te, β-Te, and γ-Te, among which α-Te and β-Te are the most stable phases³³. These theoretical reports also indicate that few-layer Te acquires the α phase, while monolayer Te exhibits the β phase. In our work, morphological analysis, Raman spectra, and AFM all reveal the presence of few-layered Te, which indicates that the as-synthesized Te is α phase (simulated structure is shown in **figure S1h**).

Understanding Alkalization of Te using In-Situ TEM Supported by DFT

In-situ TEM has proved to be successful in understanding the major electrochemical mechanisms³⁴⁻³⁵ (i.e., intercalation, alloying, and conversion) that an anode material could undergo during ion insertion/extraction. Especially for alloying/de-alloying reactions, in-situ TEM provides useful information related to volume expansion, change in morphology, and change in crystallinity that the alloying material undergoes³⁴. In this work, we used in-situ TEM to study the alloying of Te with Li, Na as well as K. **Figure S2** shows a schematic of the in-situ TEM setup used to study the alkalization (lithiation/sodiation/potassiation) of few-layer Te, wherein the corresponding alkali metal (Li/Na/K) was used as the counter electrode, naturally grown metal oxide layer (i.e., lithium oxide, sodium oxide or potassium oxide) as a solid-state electrolyte, and Te as the working electrode with gold (Au) or tungsten (W) as the current collectors. A constant bias voltage ($\sim 3\text{V}$) is applied to initiate insertion of metal ions into Te. To understand the alloying mechanism, TEM images were taken during the alkalization of Te at different time intervals. The real-time TEM imaging indicates that the few-layer Te flake gradually slides and expands during Li insertion (**figure 1a-d, Movie S1**). No significant de-lamination of Te from the W current collector was observed. Surprisingly, unlike other alloy-based materials, Te expands almost “isotropically” in both x ($\sim 11\%$) and y directions ($\sim 10\%$) till full lithiation³⁵⁻³⁸. SAED and theoretical calculations were employed to understand the phase information of the alloyed product (i.e. Li_xTe). Te can form three different alloy compositions with Li (LiTe_3 , Li_2Te , and Li_3Te). SAED pattern of pure Te and Li_xTe is shown in **figure 1e-f**, wherein pure Te shows a bright spot related to (100) plane with d spacing of $\sim 3.9 \text{ \AA}$. In addition, a diffused halo is discernable in the background, which is attributed to oxidation (**figure S1f**) of Te, which is unavoidable in hydrothermal synthesis. Oxidation of Te was also verified by EDS mapping (**figure S3**). The partial oxidation of Te also explains the rounded flake edges as-observed in TEM. The SAED pattern of Li_xTe shows three different bright spots at d spacing of $\sim 3.8 \text{ \AA}$, 3.27 \AA , and 2.09 \AA which matches well with the diffraction plane (111), (311), and (200) of Li_2Te , respectively. Interestingly, the diffraction pattern of Li_2Te did not exhibit rings, confirming that the lithiation of Te leads to the formation of a “crystalline” Li_2Te alloy. This is a striking result since almost all of the known alloy-based anode materials, such as Si, Sn and P, form either polycrystalline or amorphous materials on lithiation^{25, 26}. To check for reproducibility, the SAED analysis was repeated at several locations on the alloyed sample, which confirmed the single-crystalline property of Li_2Te . Further investigation is needed to understand this unexpected behavior, which will be discussed later in this article.

We used first-principles density functional theory (DFT) calculations to calculate the formation energy per Te atom of all the possible alloys, among which Li_2Te showed a higher formation energy (-3.19 eV) as compared to LiTe_3 (-0.38 eV) and Li_3Te (-3 eV) (**figure S4**). This indicates that Li_2Te is the expected alloy, which is consistent with our SAED results. Volume expansion due to alloy formation was theoretically calculated ($\sim 175.80\%$) which indicates that 2-D Te expands primarily in the z-direction ($\sim 119\%$) (**figure S7**). A similar set of studies were employed to study sodiation of Te. **Figure 1g** shows pure Te before sodium insertion and **figure 1j** shows fully sodiated tellurene (Na_xTe). The different time scale in Na insertion in comparison to Li may be due to variation in size or thickness of the Te flake that was used or differences in the diffusion rate of ions. Unlike Li insertion, Te expands “anisotropically” in the x ($\sim 20\%$) and y ($\sim 8\%$) directions until full sodiation (**figure 1g-j**,

Movie S2). SAED pattern of pure Te confirms its single-crystal property before insertion of Na, whereas SAED pattern of Na_xTe shows diffused rings with bright spots at d spacing of $\sim 4.5 \text{ \AA}$, 3.15 \AA , 2.59 \AA , and 2.22 \AA which matches with the diffraction plane (111), (200), (220), and (311) of Na_2Te , respectively (**Figure 1k-l**). The appearance of diffused rings indicates that the alloying of Te with Na leads to the formation of polycrystalline Na_2Te . Formation energy per Te atom was calculated (**figure S5**) for all possible stable alloys of Te with Na (NaTe_3 , NaTe , and Na_2Te) among which Na_2Te showed higher formation energy (-2.83 eV) then NaTe_3 (-0.55 eV) and NaTe (-1.48 eV), which is consistent with the SAED characterization. Volume expansion of Te during sodiation (**figure S7**) was $\sim 286.5\%$, with the primary expansion occurring in the z-direction ($\sim 190\%$).

In the case of potassiation, Te expands even more anisotropically, in the x-direction ($\sim 40\%$) and y-direction ($\sim 15\%$), when compared to sodiation (**figure 1m-p, Movie S3**). SAED pattern of potassiated Te (K_xTe) shows various diffused rings with few bright spots at d spacing of $\sim 4.14 \text{ \AA}$, $\sim 2.45 \text{ \AA}$, $\sim 2.08 \text{ \AA}$, and $\sim 1.62 \text{ \AA}$ which matches with the diffraction plane (111), (311), (400), (422) of K_2Te , respectively (**figure 1q-r**). The presence of diffused rings indicate that the K_2Te product is polycrystalline. K_2Te showed higher formation energy per Te atom (-3.09 eV) then other stable alloys such as KTe (-1.71 eV), KTe_3 (-0.19 eV), K_2Te_3 (-1.24 eV) and K_5Te_3 (-2.69 eV) (**figure S6**) which confirms that the potassiation of Te leads to the formation of K_2Te . Volume expansion during alloy formation from Te to K_2Te was $\sim 474.74\%$ (**figure S7**), with a massive volume expansion in the z-direction ($\sim 280\%$). From the above results, it is evident that alkali (A) ion (Li/ Na/ K) insertion into few-layer Te led to the formation of an A_2Te (Li_2Te , Na_2Te , K_2Te) alloy wherein the alloyed material crystallinity changed from single-crystal (for Li_2Te) to poly-crystal (for Na_2Te and K_2Te). The volume expansion in the material followed an increasing trend with increase in size of A from $\sim 175\%$ for Li to $\sim 474\%$ for K.

Discussion

Adsorption and Charge Transfer Analysis

DFT calculations were used to study the adsorption, charge transfer, and diffusion of alkali ions in few-layer Te. First, we studied the surface loading of Li/Na/K on 2-D Te sheets. In the second step, we investigated the diffusion of these ions “across” and “along” the belts of Te sheets (**figure 2a**). Optimized few-layer (4 layers) of Te (**figure S8a-c**) acquires the α phase, consistent with previous studies. Unlike other 2-D materials (e.g. graphene, MoS_2 or WS_2), the Te structure is highly anisotropic such that a Te atom is bonded to another Te atom only in one direction (along-belt direction). Multilayer Te has an ABAB stacking with an interlayer distance of $\sim 4.44 \text{ \AA}$. Within a layer, Te atoms make two bonds with other Te atoms with bond length ranging from 2.83 \AA (Te1-Te2) to $\sim 2.9 \text{ \AA}$ (Te1-Te3) and width of the belt is $\sim 4.43 \text{ \AA}$ (distance between Te1-Te4) (**figure S8d**). The corresponding bond angle ranges from ~ 101.3 to 101.8° . After the structural optimization of Te, Li/Na/K ions were sampled at different sites on the top surface of Te and allowed to relax. Our calculations indicate that the space between two belts provides stronger binding site for ions (**figure S9**). Distances between Li and the closest Te atoms are $\sim 2.72 \text{ \AA}$ (Li-Te1), $\sim 2.75 \text{ \AA}$ (Li-Te2), and $\sim 2.82 \text{ \AA}$ (Li-Te3) (**figure S9a-c, Table S1**).

In case of Na, distances are ~ 3.05 Å (Na-Te1), ~ 3.12 Å (Na-Te2), and ~ 3.09 Å (Na-Te3) (**figure S9d-f, Table S1**). For K, distances increase further and are ~ 3.41 Å (K-Te1), ~ 3.61 Å (K-Te2), and ~ 3.4 Å (K-Te3) (**figure S9g-i, Table S1**). It is to be noted that no significant disruptions were observed due to ion adsorption on the surface of Te. Energy shift of alkali-ion/Te complex with vertical distance of the alkali ion to the Te surface was also calculated (**figure S10**). The energy of the system remained constant beyond 7 Å but showed a rapid decline below 6 Å, which indicates a strong interaction between alkali atoms and Te and confirms the absence of any energy barrier for the loading process. The binding energy of Li/Na/K (E_b) on the surface of the 2-D Te sheet was calculated using the following equation:

$$E_b = E_{Te-Li/Na/K} - E_{Te} - \mu_{Li/Na/K}$$

where, $E_{Te-Li/Na/K}$, E_{Te} , and, $\mu_{Li/Na/K}$ refer to total energies of Li/Na/K adsorbed on Te, Te, and the chemical potential of Li/Na/K atom, respectively. The chemical potential of alkali atoms was calculated in two ways: (1) considering a single isolated atom in a cell (μ_{atom}), and (2) considering the bulk phase of alkali metal (μ_{bulk}). The conventional view is to calculate E_b by considering a single isolated alkali atom. However, recent reports suggest that considering a bulk phase of alkali atom is more appropriate (especially in the battery field)^{39,40}. Herein, we have considered both the methods and observed that the binding energies of Li/Na/K with the surface of Te are all negative (**figure 2b, Table S1**) which indicates a favorable interaction. However, we do observe a difference in the binding energy trend wherein Li adsorbed more strongly (-2.56 eV) than other alkali atoms (-1.98 eV for Na and -2.1 eV for K) based on μ_{atom} method, but with the μ_{bulk} method, K adsorbed more strongly (-1.028 eV) then Li (-0.55 eV) and Na (-0.56 eV) (**Table S1**).

Similar calculations were repeated with alkali atoms (Li/ Na/ K) in between two layers (**figure S11, Table S1**). No significant disruption was observed in the case of Li inside two layers (**figure S11a-c**). However, significant damage and complete disruption of the upper layer was observed in the case of Na/K due to their larger size when compared to the Li atom (**figure S11d-i**). This indicates that delamination of the electrode is less severe for a Te anode with Li insertion as opposed to Na or K. Similarly, the magnitude of the binding energy of Li when placed between two layers did not decrease significantly (~ 0.05 eV) in comparison with Na (~ 0.36 eV) and K (~ 0.5 eV), which suggests that the thermodynamic barrier for the transport of Li through Te layers is much lower than for Na and K. Hirschfeld I-charge analysis was further employed to illustrate the spatial charge distribution between alkali atoms and Te. Charge deficiency on alkali atoms and excess charge on Te indicates charge transfer from alkali atoms to the surface of Te. Hirschfeld I-charge analysis indicates that Li transfers $0.8 e^-$ to Te, which is lower than Na ($0.911 e^-$) and K ($1.451 e^-$) (**figure 2b**). This is due to the low ionization energy of K in comparison with Na and Li. A similar trend in charge transfer was also observed for alkali atom adsorption in-between Te sheets. The effect of alkali ion absorption on Te was further evaluated by calculating the total density of states (TDOS). The TDOS of pristine Te shows a bandgap of ~ 0.3 eV with Fermi level close to the valence band indicating p-type semiconducting behavior of Te, which is in agreement with previous reports (**figure S12a**). On alkali ion adsorption over Te, the Fermi level shifts inside the conduction band, thus showing metallic behavior due to n -type doping induced by the alkali atom (**figure S12b-d**). Our DFT calculations therefore indicate effective absorption of alkali ions on Te, with significant charge transfer and semiconductor to metallic transition, all favorable characteristics for a battery electrode material.

Diffusion of Alkali Atoms on Monolayer Te

The mobility of alkali-ions inside the electrode material not only governs the rate performance of the battery but also helps us in understanding the evolution of electrode structure during the alloying reaction. NEB calculations were employed to study diffusion barrier energy of all three alkali ions in the “along-belt” and “across-belt” directions of single-layer Te and in the interior of few-layered Te (Methods). After establishing the most stable site for alkali ion adsorption on single-layer Te, we studied migration of the alkali ion from one stable site to the next for three possible pathways: (1) across-belt, (2) along-belt, and (3) through the single-layer Te sheet (**figure S13**). While studying migration across-belt, we observed that all three alkali atoms showed one major peak at the same reaction coordinate with barrier energy for Li (0.19 eV, **figure S13a**), Na (0.19 eV, **figure S13b**) and K (0.13 eV, **figure S13c**). Such difference can possibly arise due to the larger distance of K atom from Te surface (4.07 Å) in comparison with Li (2.92 Å) and Na atom (3.47 Å), which can lead to less hindrance for Te atoms during K migration. However, in case of “along-belt” diffusion, barrier energy for Li migration (~ 0.2 eV, **figure S13a**) is less than Na (~ 0.32 eV, **figure S13b**) and K (~ 0.33 eV, **figure S13c**) and exhibits a peak at a different reaction coordinate in comparison to Na and K. These differences arise due to the different path that the Li atom has undertaken while migrating from one stable site to another during along-belt diffusion. Na and K migrate along the path where “cliff-top” Te atoms are present between adjacent grooves. However, Li chooses a different path, wherein it initially goes through the Te sheet, migrates to the other side, and then comes back out of the Te sheet enabling it to avoid encounters with cliff-top Te atoms, leading to a lower barrier energy in comparison with other alkali atoms. Such movement is restricted for Na and K because of their larger size compared to Li; barrier energy for movement through Te is much higher for Na (0.15 eV, **figure S13b**) and K (0.5 eV, **figure S13c**) compared to Li (0.04 eV, **figure S13a**). Once the energy barriers are known, the diffusion constant (D) can be predicted using the Arrhenius equation:

$$D \sim \exp\left(\frac{-E_a}{k_b T}\right)$$

where E_a is the activation energy (energy barrier), k_b and T are Boltzmann constant and temperature (considering room temperature ~300 K). The ratio of diffusion mobility “across-belt” and “along-belt” is around ~1 for Li, but Na and K diffusion mobility “across-belt” is ~148 times and ~2191 times higher than “along-belt”, respectively. This indicates that the migration of Li atoms on the Te surface is quite isotropic. Given that Te has an anisotropic structure, one would expect non-uniform spatial diffusion for alkali atoms. While such anisotropic diffusion is indeed predicted for Na and K, this is surprisingly not the case for Li, enabling it to diffuse “isotropically” along the 2-D Te sheet.

Diffusion of Alkali Atoms within Few-Layered Te

To manage the computational cost, we considered a unit cell comprised of three layers of monolayer Te, that were stacked in AB sequence and alkali atoms were placed in the interior of the multilayer stack (**figure S11**). Migration of alkali atoms was studied both “across-belt” and “along-belt” after optimizing the most stable adsorption site in the interior

of the stack. When sampling Na and K atoms in the interior of the layered Te, the adjacent layers get deformed, which affects the diffusivity of Na and K. In the case of Li, no such damage was observed. Unlike in single-layer Te, migration of Li atom “across-belt” in layered Te shows two distinct peaks, which are presumably caused by presence of additional binding sites provided by the first layer (**figure 2c**). The energy barrier for Li transport was ~ 0.13 eV, which is much lower than for Na (~ 0.32 eV; **figure 2d**) and K migration (~ 0.62 eV; **figure 2e**). The high energy barrier for Na and K arises due to their much larger atomic size when compared to Li. In addition, the adjacent layers in few-layered Te can provide significant hindrance to restrict the migration of Na and K.

While studying “along-belt” diffusion, a surprising trend in energy barrier was observed in case of Li and Na atoms, wherein the energy barrier first decreases and then increases to a certain value. Such a decrease in energy barrier is likely due to the presence of an even more stable site at the bottom of the first layer (global minimum), as compared to the starting site (local minimum). No such trend was observed for the K atom. As for the single-layered Te case, the energy barrier for Li “along-belt” diffusion for few-layered Te is exactly equal to “across-belt” diffusion (~ 0.13 eV) and much lower than that of Na (~ 0.37 eV) and K (~ 0.67 eV). The lower diffusion energy barrier for Li indicates that Te based Li-ion batteries will have superior high-rate performance when compared with Te based Na-ion and K-ion batteries. Using the Arrhenius equation, one can show that similar to single-layer Te, the diffusion mobility of Li in few-layered Te is also highly isotropic, whereas Na and K atoms exhibit significantly anisotropic diffusivity.

Ab-Initio Molecular Dynamics

Since the computational burden of DFT limits its application to larger simulation cells, we utilized ab-initio molecular dynamics (AI-MD) to explore the diffusion properties of alkali species in multi-layer Te systems. More specifically, $\text{Te}_{48}\text{A}_{12}$ and $\text{Te}_{48}\text{A}_{24}$ (A = Li/Na/K) configurations were used, wherein the $\text{Te}_{48}\text{A}_{12}$ and $\text{Te}_{48}\text{A}_{24}$ structures were initially optimized at 0.1 K and then simulated at 300 K for ~ 10 picoseconds (ps) (**figure S14**) (details in Methods). As expected, such a high concentration of alkali atoms will start disrupting the 2-D Te structure, which is an indication of the onset of the alloying process and if given sufficient time, will lead to the alloyed product. Our main aim during AI-MD was to study the diffusion property of alkali atoms during the alloying process, and to quantify this, we computed the average mean square displacement (MSD) (**figure 3**). While comparing MSD results for $\text{Te}_{48}\text{Li}_{12}$, $\text{Te}_{48}\text{Na}_{12}$, and $\text{Te}_{48}\text{K}_{12}$, we observe that the MSD in the x-direction (across-belt) and y-direction (along-belt) for Li atoms were almost same during the alloying process (**figure 3a**). By contrast, deviation in MSD in x- and y- directions were quite pronounced for Na atoms (**figure 3b**) which further increases for K atoms (**figure 3c**). In the case of $\text{Te}_{48}\text{Na}_{12}$, and $\text{Te}_{48}\text{K}_{12}$, we observe that the MSD displacement is higher in the y-direction (along-belt) as compared to x-direction (across-belt), which can be due to the lower density of Te-Te bonds along the y-direction. A similar observation was also made when we increased the number of alkali atoms to 24 (**figure 3d-f**). Isotropic displacement of Li during the alloying indicates that Li atoms reach every Te atom with equal probability, which leads to the formation of ordered alloyed products. However, in the case of Na and K, one direction of movement is preferred, which indicates that some Te atoms (which lie in a preferred direction) will encounter an abundance of Na or K atoms, while others in a non-

preferred direction will experience a scarcity of Na or K atoms. This leads to the unordered formation of the alloyed product, with resultant loss in crystallinity. In this way, the DFT and AI-MD simulation results back up our in-situ TEM observations, and provide fundamental insight to explain the differences in the crystalline order of Li_2Te (single-crystal), Na_2Te (poly-crystal) and K_2Te (poly-crystal). Having understood the alloying process of Te with various alkali metals and having developed an in-depth understanding of the alloying phases and compositions, the stage is now set for the electrochemical testing of Te-based Li, Na and K-ion batteries.

Electrochemical Testing of Te Batteries

A half-cell LIB was assembled by coating Te sheets on a copper foil current collector with a Li metal foil as the counter electrode and 1M lithium hexafluorophosphate in ethylene carbonate-diethylene carbonate as the electrolyte. For the sodium ion battery (SIB), Na foil was used as counter electrode and the electrolyte was 1M sodium perchlorate in ethylene carbonate-propylene carbonate, while for the potassium ion battery (KIB), we employed a K foil with 1M potassium hexafluorophosphate in ethylene carbonate-diethylene carbonate as the electrolyte (Methods). Top and cross-section SEM imaging of the electrode indicates that the structure of Te sheets remains intact during the coating process. The typical Te electrode thickness was measured to be $\sim 10\ \mu\text{m}$ (**figure S15**). To understand alkali ion insertion, cyclic voltammetry (CV) was performed at a scan rate of $\sim 0.05\ \text{mV/sec}$ over 4 cycles in the voltage range of 0.03-3V (for Li), 0.03-2.75V (for Na), and 0.03-2.5V (for K). During 1st cycle discharge, CV for the Te-based LIB (**figure 4a**), shows a prominent discharge peak at $\sim 1.6\ \text{V}$, which is shifted to $\sim 1.65\ \text{V}$ in subsequent cycles. This indicates that the alloying of Te with Li occurs primarily at $\sim 1.65\ \text{V}$. In the charging process, a prominent peak appeared at $\sim 1.97\ \text{V}$, indicating that the de-alloying reaction occurred at $\sim 1.97\ \text{V}$. In the first cycle, a prominent peak is also observed at $\sim 2.3\ \text{V}$, but this is related to the solid electrolyte interface (SEI), since it diminishes significantly in subsequent cycles. Similar CV scans for the SIB and KIB configurations (**Figures S16-17**) indicate that the alloying reaction of Te with Na takes place primarily at $\sim 1.55\ \text{V}$, while a stepwise dealloying is observed at $\sim 1.69\ \text{V}$ and $\sim 2.09\ \text{V}$. For KIB, relatively broad peaks centered at $\sim 1.92\ \text{V}$, $\sim 1.03\ \text{V}$, $\sim 0.36\ \text{V}$ during discharge are observed, which are attributed to stepwise alloying of Te with K, while peaks at $\sim 0.38\ \text{V}$, $0.84\ \text{V}$, and $\sim 1.94\ \text{V}$ correspond to step-wise de-alloying. The absence of prominent (sharp) peaks for KIBs is expected and is attributed to the relatively slow diffusion of K ions due to their larger size. To verify this, we carried out galvanostatic intermittent titration technique (GITT) characterization of the various cells. The measured diffusion coefficient of Li in Te is in the range of $10^{-14} - 10^{-15}\ \text{cm}^2\ \text{s}^{-1}$ which is one order of magnitude higher than Na ($10^{-15} - 10^{-16}\ \text{cm}^2\ \text{s}^{-1}$) and two orders higher than K ($10^{-16} - 10^{-17}\ \text{cm}^2\ \text{s}^{-1}$) (**Figure S18**). The voltages for alloying/dealloying of Li/Na/K with Te as obtained from GITT was also consistent with the CV results discussed above.

Next, we carried out galvanostatic charge-discharge cycling for the Te based batteries at 0.1C for 50 cycles (**figure 4b**). After SEI formation, the Te based Li battery (Te||Li) showed an initial gravimetric specific capacity of $\sim 350\ \text{mAh g}^{-1}$ (theoretical upper limit for Li_2Te is $\sim 420\ \text{mAh g}^{-1}$). However, a significant drop in specific capacity was observed within the first 20 cycles to $\sim 120\ \text{mAh g}^{-1}$ after which capacity remained fairly constant up to 50 cycles ($\sim 105\ \text{mAh g}^{-1}$). Such rapid capacity fade is common in alloying anodes and is related

to volume expansion (~175.80%) in Te, which causes pulverization and delamination of the active material. The capacity fade is even more severe for Na and K. After 50 cycles, Te||Na and Te||K displayed specific capacities of only ~60 mAh g⁻¹ and ~42 mAh g⁻¹, respectively. The superior performance of Li over Na and K is understandable given that the volume expansion of Te when alloyed with Na (~286.5%) and K (~474.74%) is much larger than for Li (~175.80%). Initial Columbic Efficiency (CE) in Te||Li was ~40%, which is higher than Te||Na (~30%) and Te||K (~10%). Over 50 cycles, the CE of Te||Li and Te||Na reached ~100%, whereas the CE of Te||K was still only ~90%. This is presumably due to the larger size of K (2.8 Å vs 1.82 Å for Li and 2.22 Å for Na), which could impede the dealloying process. To address the capacity fade issue, we created composite electrodes of Te with graphene, which displayed much better cycle stability and good rate capability (**Figure S19**). This is due to the ability of graphene to act as a buffer layer to suppress the stress induced pulverization and delamination of Te. The graphene coating on Te can also help with creating a more stable SEI layer and lowering the charge transfer resistance of the battery.

From a gravimetric perspective, Te offers no significant advantage over traditional graphite. However, volumetrically the picture is very different. The theoretical maximum volumetric capacity of Te in LIBs is ~2620 mAh cm⁻³ which is ~6-8 times higher than graphite. To maximize volumetric capacity, we performed calendaring (Methods) to densify the Te electrode and avoided the use of graphene as a buffering material. Calendaring of Te did not affect its morphology but decreased the electrode thickness by ten-fold (~1 µm) as evidenced by cross-section SEM (**figure S20**) and Energy Dispersive X-ray (EDX) analysis (**figure S21**). The calendared Te electrode showed a high initial volumetric charge capacity of ~2000 mAh cm⁻³ (~380 mAh g⁻¹). In the absence of the graphene buffering material, capacity fade during initial cycles is unavoidable. In spite of this, the volumetric capacity stabilizes to ~700 mAh cm⁻³ (~150 mAh g⁻¹) after 50 cycles (**figure 4c**) which is ~2-times that of commercial graphitic anodes¹⁵ (330-430 mAh cm⁻³). The voltage profile for the calendared Te electrode (**figure 4d**) shows similar plateaus at the same voltages as what was observed for the non-calendared Te (**figure S22**), confirming that the alloying/de-alloying process is unaffected by the calendaring. It should be noted that the volumetric capacity numbers that we report are calculated based on the volume of the “entire electrode” including the active (Te) material, carbon black and binder. Such calendared Te electrodes (either by themselves or as composites with graphite) show significant potential for LIB applications involving energy storage in compact spaces, where the maximum amount of energy must be packed into a limited volume.

Methods

Te Material Synthesis: A one-step hydrothermal method was used to synthesize Te. Initially, ~100 mg of sodium tellurite (Na₂TeO₃) and ~345 mg of polynyl pyrrolidone (PVP, k17) were mixed in ~33 ml of deionized water at room temperature for ~10 mins followed by addition of ~1ml hydrazine hydrate (N₂H₄, 85% wt/wt%) and ~2 ml ammonia solution (NH₄ 25% wt/wt%). The mixture was then transferred to a Teflon lined stainless steel autoclave (50ml) which was then heated at ~180 °C for ~40 hrs. This led to the formation of a silver-grey colored powder, which was washed several times with de-ionized water using filtration method to remove any ion contaminants. To remove PVP molecules adsorbed on the tellurene surface, acetone (~3ml) was added to the Te solution (~1ml) and kept for several

hours at room temperature. The solution was then washed several times with de-ionized (DI) water to obtain the purified 2-D Te sheets. For Te-graphene composites, as-synthesized Te sheets (~40 mg) and as-received graphene powder (~120 mg) were separately mixed in anhydrous NMP at a concentration of ~0.5 mg/ml and ~1 mg/ml respectively and was bath sonicated for ~30 mins. Te and graphene solutions were then mixed in various proportions and further bath sonicated for ~1hr, and then filtered out using vacuum filtration. The resultant product was then dried at ~70 °C under vacuum overnight which leads to the removal of any NMP traces. This led to the formation of the Te-graphene composite powder.

Te Electrode Synthesis: As synthesized Te was mixed with super P carbon black and polyvinylidene fluoride (PVDF) binder in 70:20:10 % proportion by weight. Few drops of NMP were carefully added into the mixture which was then stirred for ~20 mins at ~2000 rpm. This led to the formation of silver-grey colored slurry, which was coated over a copper foil current collector substrate and dried overnight at room temperature. The Te-graphene electrode was synthesized using a similar procedure with an alteration in a weight proportion of Tellurene-graphene, super P carbon black, and PVDF binder (80:10:10 % was used). Calendaring was done using MTI-MSK_HRP MR100DC machine, wherein as-fabricated electrodes were placed in-between two fixed rollers (separation distance was set at 1 micron). In order to obtain uniform thickness, calendaring was repeated multiple times.

Li, Na, and K - Half Cell Measurements: 2032-type coin cells were assembled wherein Li, Na and K metal was used as a reference electrode for LIBs, SIBs, and KIBs half-cell measurement, respectively. Initially, as prepared electrodes were punched into circular disks with an area of ~1.27 cm². Mass loading (Te + super P carbon + PVDF) was around ~2 mg. In the case of LIBs, commercially available 1.0 M lithium hexafluorophosphate (LiPF₆) in ethylene carbonate (EC): diethyl carbonate (DEC), 1:1 volume ratio, was used as the electrolyte. In the case of KIBs, 0.9 M potassium hexafluorophosphate (KPF₆) in EC: DEC (1:1 v/v) was synthesized and used as an electrolyte. 1.0 M sodium perchlorate (NaClO₄) in EC: propylene carbonate (PC) (1:1 v/v) was synthesized and used as an electrolyte for SIBs. Celgard 2340 polypropylene (PE) membrane was used as a separator for both LIBs and KIBs, whereas the Whatman glass fiber membrane was used for SIBs. All batteries were assembled in an argon-filled glove box (MBraun Labster) with moisture and oxygen level < 0.1 ppm. Charge/Discharge measurement was done using Arbin BT200 battery test equipment and within voltage window of 0.03-3V, 0.03-2.75V, and 0.03-2.5V for LIBs, SIBs, and KIBs, respectively. GITT was also performed using the same equipment and voltage window. Gamry instrument was used to perform cyclic voltammetry (CV) of all the battery cells in their respective voltage windows.

DFT Calculations: Density functional theory (DFT) computations were carried out with the Vienna Ab-initio Simulation Package (VASP) using the projector-augmented-wave (PAW) method. All the exchange-correlation effects were described by the Perdew–Burke–Ernzerhof (PBE) functional within the generalized gradient approximation (GGA). To account for the van der Waals (vdW) interactions resulting from the fluctuating charge distributions, Grimme's empirical dispersion correction scheme was employed (DFT-D3 method in

VASP). A kinetic energy cutoff of 500 eV is used to generate a plane-wave basis set and k -points were sampled using a gamma point centered $4 \times 4 \times 1$ Monkhorst–Pack mesh. The geometry optimization was run until the self-consistent field (SCF) energies and maximum forces on each atom were below a threshold value of 10^{-5} and $0.05 \text{ eV}\text{\AA}^{-1}$, respectively. The conjugate gradient algorithm as implemented in VASP (IBRION=2) was utilized to relax all structures. In this work, we consider a monolayer (48 Te atoms) and a 4-layer (36 Te atoms) β tellurene supercell. The supercell dimensions for the 4-layer Te system in x and y directions are 8.86 \AA and 11.87 \AA , respectively. However, for the monolayer system, cell dimensions are relatively larger with $x=17.72 \text{ \AA}$ and $y=23.73 \text{ \AA}$, and only the gamma point is considered for the calculation. A vacuum of over 15 \AA in the z -direction is used to avoid unwanted interaction between periodic images. To understand the diffusion of alkali (Li/Na/K) atoms in monolayer/4-layer tellurene, we use DFT in conjunction with climbing image nudged elastic band (CI-NEB) method to investigate the migration paths and energy barriers of alkali atom moving from one stable site to another in x/y or along the z -directions. Further, we evaluate Hirschfeld-I charges to understand the charge distribution or transfer during Li/Na/K atom binding with the Te surfaces.

Ab-Initio Molecular Dynamics Calculations: The Ab-initio Molecular Dynamics simulations were performed using the Vienna ab initio simulation package (VASP). First, the lattice constants of the configurations studied, namely: $\text{Te}_{48}\text{Li}_{12}$, $\text{Te}_{48}\text{K}_{12}$, $\text{Te}_{48}\text{Na}_{12}$, $\text{Te}_{48}\text{Li}_{24}$, $\text{Te}_{48}\text{K}_{24}$, $\text{Te}_{48}\text{Na}_{24}$, were optimized. The structures are then relaxed by initial geometry optimization through DFT calculations, which is followed by the AIMD run. To study the directional diffusion characteristics, mean square displacement of the diffusing Li, K, and Na atoms is calculated from AIMD trajectories sampled for runtimes of 5 ps. An isokinetic ensemble (NVT) is adopted for the simulations, where the ionic temperature (300K) is controlled by the Nose-Hoover thermostat. A time step of 1 fs has been used for the integration of the equations of motion. The ion-electron interactions are presented with the projector augmented wave (PAW) method, and the exchange-correlation effects are determined by the generalized gradient approximation (GGA) with the Perdew-Burke-Ernzerhof (PBE) functional. An energy cutoff of 350 eV is considered for the plane-wave basis and a $4 \times 4 \times 1$ Monkhorst-Pack scheme k -point grid is adopted for the systems studied.

Materials Characterization: Morphology of Tellurene sheets and electrodes were obtained using Carl Zeiss Supra 55 field-emission scanning electron microscope with beam energy of $\sim 2.5 \text{ kV}$. Cross section of the tellurene electrodes before and after calendaring was obtained using gallium focused ion beam (FIB) sputtering at $\sim 30 \text{ keV}$ using FEI VERSA three-dimensional dual beam system. Coarse sputtering and final cleaning of the cross section were carried out at $\sim 15 \text{ nA}$ and $\sim 1 \text{ nA}$ beam current, respectively. Deposition of platinum through ion- beam allowed us to protect the electrode surface from damage due to sputtering at higher ion beam current. SEM images of cross section were taken at $\sim 2.5 \text{ kV}$ and at a $\sim 52^\circ$ tilt. TEM was done using JEM2100F operating at 200 kV . STEM-EDS mapping was done using EOL JEMARM200CF equipped with a 200 KV cold field emission electron gun and an Oxford X-max 100TLE windowless SDD X-ray detector. Thickness of as synthesized tellurene was obtained through AFM (Bruker, Innova). Raman spectroscopy was obtained through back

scattering geometry using a single monochromator with a Reinshaw in Via microscope equipped with cooled (-70°C) CCD array detector (1024 x 256 pixels) and edge filter. XRD data was obtained through Bruker D2 PHASER using Cu/K α radiation ($\lambda = 1.5418 \text{ \AA}$) at 40 kV and 30 mA. XPS was obtained using PHI 5000 versa probe system using Al K α radiation ($\sim 1486 \text{ eV}$)^{18, 41}.

Data Availability

All relevant data are available from the corresponding author upon request.

Acknowledgements

This work was supported by the USA National Science Foundation (award numbers 1608171 and 1922633). N.K. also acknowledges funding support from the John A. Clark and Edward T. Crossan endowed chair professorship at Rensselaer Polytechnic Institute (RPI). S.O.K. was financially supported by the National Creative Research Initiative (CRI) Center for Multi-Dimensional Directed Nanoscale Assembly (2015R1A3A2033061) through the National Research Foundation of Korea (NRF). R. S-Y. and Y. Y. acknowledge the financial support from NSF CBET-1805938. This work made use of instruments in the Electron Microscopy Service (Research Resources Center, UIC). L. W. W. acknowledge support from Assistant Secretary for Energy Efficiency and Renewable Energy of the U. S. Department of Energy under Battery Materials Research (BMR) program. The theoretical work in this research used the resources of the National Energy Resources Scientific Computing Center (NERSC) that is supported by the office of Science of the U. S. Department of Energy.

Authors Contributions

R.J. carried out the synthesis and characterization of the Tellurene/graphene composite. R.J. also designed and conducted the battery test. Y.Y. and R.S.Y. conducted in-situ TEM experiments. Y.S. S.B., D.M. and R.K. performed the theoretical calculations. D.W., A.Y., X.W. and M.R. carried out the synthesis and characterization of Te. H.J.L performed characterization of the Tellurene/graphene composite. D. F., Y.Y. and R.S.Y. carried out SEM, FIB-SEM, and EDX analysis. P.H. and F.H. contributed to analyzing the data related to the battery. S.O.K. contributed to analyzing the data related to Te and its synthesis. L.W.W contributed to analyzing the theoretical data. R.J. and N.K. wrote the manuscript. N.K. supervised and directed the project and contributed to analyzing the data.

Additional Information

Competing interests: The authors declare no competing interests.

Supplementary Information accompanies this paper

References

1. Li, M., Lu, J., Chen, Z. & Amine, K. 30 Years of Lithium-Ion Batteries. *Adv. Mater.* **30**, 1800561 (2018).
2. Goodenough, J. B. & Park, K.-S. The Li-Ion Rechargeable Battery: A Perspective. *J. Am. Chem. Soc.* **135**, 1167–1176 (2013).
3. Manthiram, A. An Outlook on Lithium Ion Battery Technology. *ACS Cent. Sci.* **3**, 1063–1069 (2017).
4. Li, L. *et al.* Vanadium disulfide flakes with nanolayered titanium disulfide coating as cathode materials in lithium-ion batteries. *Nat. Commun.* **10**, 1764 (2019).
5. Armand, M. & Tarascon, J.-M. Building better batteries. *Nature* **451**, 652–657 (2008).
6. Blomgren, G. E. The Development and Future of Lithium Ion Batteries. *J. Electrochem. Soc.* **164**, A5019–A5025 (2016).
7. Liu, Y., Zhu, Y. & Cui, Y. Challenges and opportunities towards fast-charging battery materials. *Nat. Energy* **4**, 540–550 (2019).
8. Manthiram, A. A reflection on lithium-ion battery cathode chemistry. *Nat. Commun.* **11**, 1550 (2020).
9. Jain, R. *et al.* Reversible Alloying of Phosphorene with Potassium and Its Stabilization Using Reduced Graphene Oxide Buffer Layers. *ACS Nano* **13**, 14094–14106 (2019).
10. Li, L. *et al.* A Foldable Lithium–Sulfur Battery. *ACS Nano* **9**, 11342–11350 (2015).
11. Wu, F., Maier, J. & Yu, Y. Guidelines and trends for next-generation rechargeable lithium and lithium-ion batteries. *Chem. Soc. Rev.* **49**, 1569–1614 (2020).
12. Obrovac, M. N. & Chevrier, V. L. Alloy Negative Electrodes for Li-Ion Batteries. *Chem. Rev.* **114**, 11444–11502 (2014).
13. Sun, Y., Liu, N. & Cui, Y. Promises and challenges of nanomaterials for lithium-based rechargeable batteries. *Nat. Energy* **1**, 16071 (2016).
14. Choi, J. W. & Aurbach, D. Promise and reality of post-lithium-ion batteries with high energy densities. *Nat. Rev. Mater.* **1**, 16013 (2016).
15. Nitta, N., Wu, F., Lee, J. T. & Yushin, G. Li-ion battery materials: present and future. *Mater. Today* **18**, 252–264 (2015).
16. Wu, W., Qiu, G., Wang, Y., Wang, R. & Ye, P. Chem Soc Rev nanomanufacturing , and device applications. 7203–7212 (2018) doi:10.1039/c8cs00598b.
17. Wang, Y. *et al.* Field-effect transistors made from solution-grown two-dimensional tellurene. *Nat. Electron.* **1**, (2018).
18. Wang, D. *et al.* Tellurene based chemical sensor. *J. Mater. Chem. A* **7**, 26326–26333 (2019).
19. Sharma, S., Singh, N. & Schwingenschlögl, U. Two-Dimensional Tellurene as Excellent Thermoelectric Material. *ACS Appl. Energy Mater.* **1**, 1950–1954 (2018).
20. Deckoff-Jones, S., Wang, Y., Lin, H., Wu, W. & Hu, J. Tellurene: A Multifunctional

- Material for Midinfrared Optoelectronics. *ACS Photonics* **6**, 1632–1638 (2019).
21. Jain, R. *et al.* Ambient Stabilization of Few Layer Phosphorene via Noncovalent Functionalization with Surfactants: Systematic 2D NMR Characterization in Aqueous Dispersion. *Chem. Mater.* **31**, 2786–2794 (2019).
 22. Jain, R. *et al.* Phosphorene for energy and catalytic application—filling the gap between graphene and 2D metal chalcogenides. *2D Mater.* **4**, 042006 (2017).
 23. Li, Q., Zhou, Q., Shi, L., Chen, Q. & Wang, J. Recent advances in oxidation and degradation mechanisms of ultrathin 2D materials under ambient conditions and their passivation strategies. *J. Mater. Chem. A* **7**, 4291–4312 (2019).
 24. Yan, J. *et al.* Excellent Device Performance of Sub-5-nm Monolayer Tellurene Transistors. *Adv. Electron. Mater.* **5**, 1900226 (2019).
 25. Wang, X. *et al.* High damage tolerance of electrochemically lithiated silicon. *Nat. Commun.* **6**, 8417 (2015).
 26. Liu, X. H. *et al.* In situ atomic-scale imaging of electrochemical lithiation in silicon. *Nat. Nanotechnol.* **7**, 749–756 (2012).
 27. Li, H., Li, J., Zaker, N., Zhang, N., Botton, G., Dahn, J. R. Synthesis of single crystal $\text{LiNi}_{0.88}\text{Co}_{0.09}\text{Al}_{0.03}\text{O}_2$ with a two-step lithiation method. *J. Electrochem. Soc.* **166**, A1956-A1963 (2019).
 28. Tang, Z., Wang, Y., Sun, K. & Kotov, N. A. Spontaneous Transformation of Stabilizer-Depleted Binary Semiconductor Nanoparticles into Selenium and Tellurium Nanowires. *Adv. Mater.* **17**, 358–363 (2005).
 29. Safdar, M. *et al.* Site-specific nucleation and controlled growth of a vertical tellurium nanowire array for high performance field emitters. *Nanotechnology* **24**, 185705 (2013).
 30. Wang, Q. *et al.* Van der Waals Epitaxy and Photoresponse of Hexagonal Tellurium Nanoplates on Flexible Mica Sheets. *ACS Nano* **8**, 7497–7505 (2014).
 31. Chen, J. *et al.* Ultrathin β -tellurium layers grown on highly oriented pyrolytic graphite by molecular-beam epitaxy. *Nanoscale* **9**, 15945–15948 (2017).
 32. Huang, X. *et al.* Epitaxial Growth and Band Structure of Te Film on Graphene. *Nano Lett.* **17**, 4619–4623 (2017).
 33. Xiang, Y., Gao, S., Xu, R.-G., Wu, W. & Leng, Y. Phase transition in two-dimensional tellurene under mechanical strain modulation. *Nano Energy* **58**, 202–210 (2019).
 34. Shang, T. *et al.* Atomic-Scale Monitoring of Electrode Materials in Lithium-Ion Batteries using In Situ Transmission Electron Microscopy. *Adv. Energy Mater.* **7**, 1700709 (2017).
 35. Jung, S. C., Choi, J. W. & Han, Y.-K. Anisotropic Volume Expansion of Crystalline Silicon during Electrochemical Lithium Insertion: An Atomic Level Rationale. *Nano Lett.* **12**, 5342–5347 (2012).
 36. Su, Q. *et al.* In Situ Transmission Electron Microscopy Observation of Electrochemical Behavior of CoS_2 in Lithium-Ion Battery. *ACS Appl. Mater. Interfaces* **6**, 3016–3022 (2014).

37. Moon, J., Park, M.-S. & Cho, M. Anisotropic Compositional Expansion and Chemical Potential of Lithiated SiO₂ Electrodes: Multiscale Mechanical Analysis. *ACS Appl. Mater. Interfaces* **11**, 19183–19190 (2019).
38. Wang, C. *et al.* Anisotropic expansion and size-dependent fracture of silicon nanotubes during lithiation. *J. Mater. Chem. A* **7**, 15113–15122 (2019).
39. Fan, X., Zheng, W. T., Kuo, J.-L. & Singh, D. J. Adsorption of Single Li and the Formation of Small Li Clusters on Graphene for the Anode of Lithium-Ion Batteries. *ACS Appl. Mater. Interfaces* **5**, 7793–7797 (2013).
40. Ling, C. & Mizuno, F. Boron-doped graphene as a promising anode for Na-ion batteries. *Phys. Chem. Chem. Phys.* **16**, 10419–10424 (2014).
41. Hundekar, P. *et al.* In situ healing of dendrites in a potassium metal battery. *Proc. Natl. Acad. Sci.* **117**, 5588 LP – 5594 (2020).

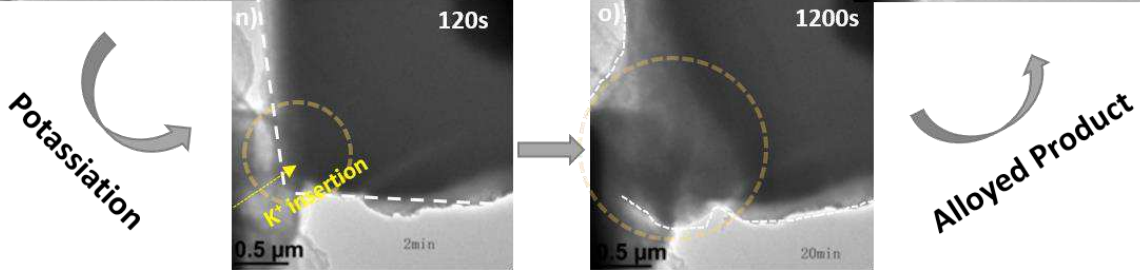
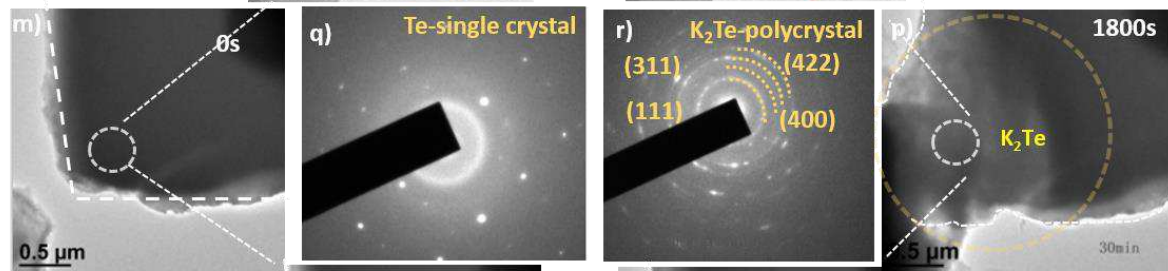
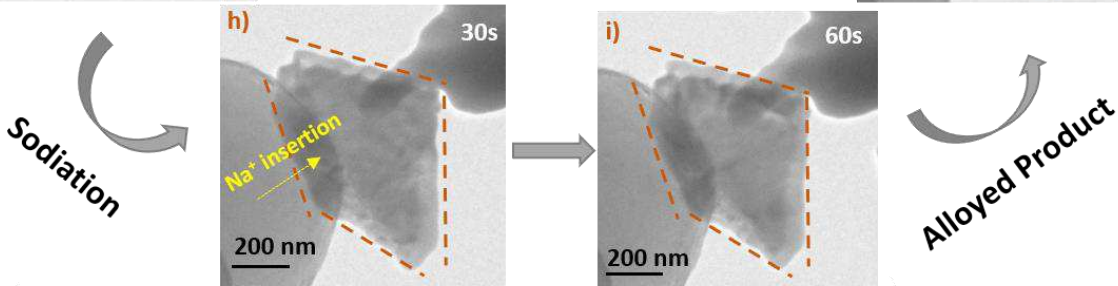
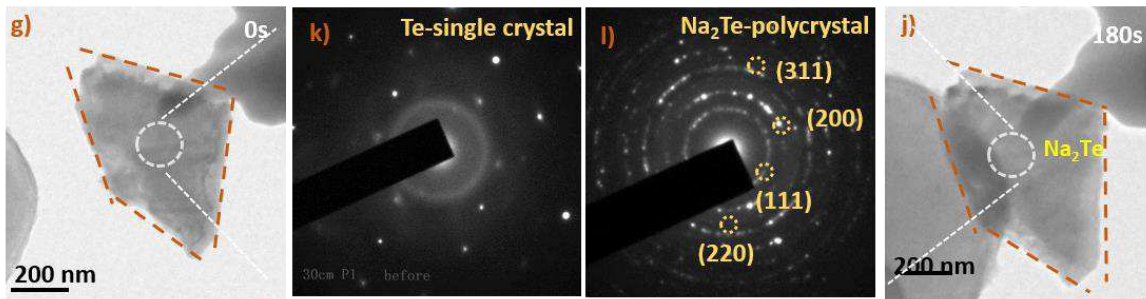
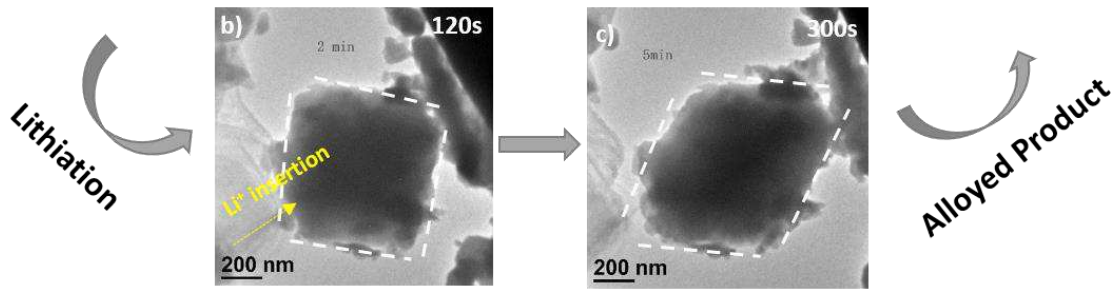
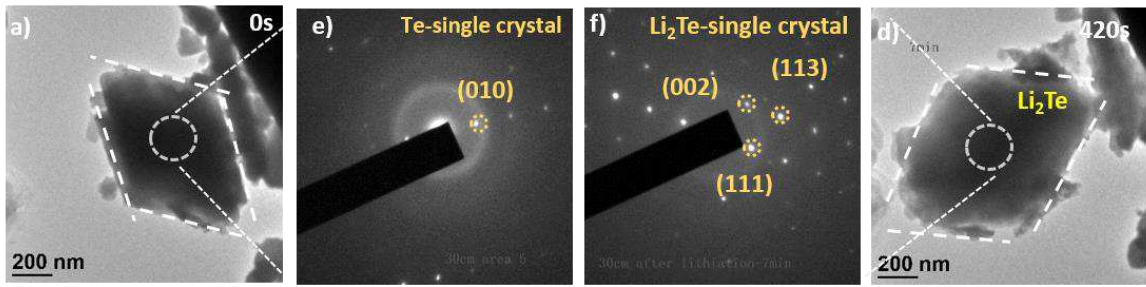


Figure 1 | In-situ TEM study of alkali ion insertion in Te. TEM images of Te (a) before (0s) and after (b) 120 s, (c) 300 s, and (d) complete (420s) lithium ion insertion. Corresponding SAED patterns of (e) pristine Te and (f) lithiated Te. TEM images of Te (g) before (0s) and after (h) 30 s, (i) 60 s and (j) complete (180 s) sodium ion insertion. Corresponding SAED patterns of (k) pristine Te and (l) sodiated Te. TEM images of Te (m) before (0s) and after (n) 120 s, (o) 1200 s and (p) complete (1800 s) potassium ion insertion. Corresponding SAED patterns of (q) pristine Te and (r) potassiated Te.

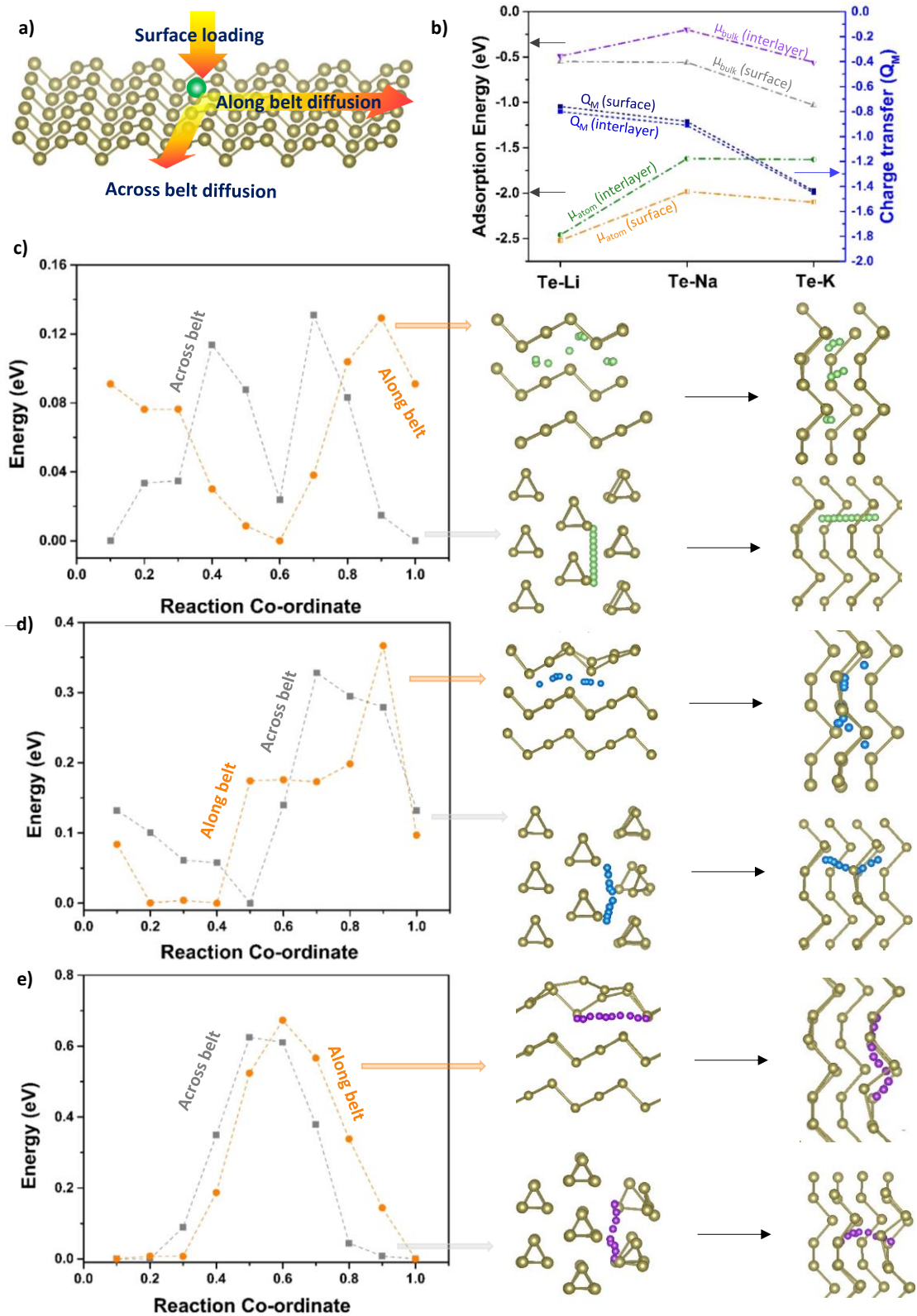


Figure 2 | DFT study of interaction between Te and alkali ions. (a) Schematic illustration of alkali atom adsorption and diffusion through the “along-belt” and “across-belt” directions. (b) Adsorption energy of different alkali atoms on the surface and in the interior of Te, calculated using μ_{atom} and μ_{bulk} method and charge transfer between alkali ions and Te sheets. (c-e) Diffusion energy barrier “along-belt” and “across-belt” for (c) Li, (d) Na, and (e) K migration in interior of few-layered Te. Corresponding simulated structures are also shown.

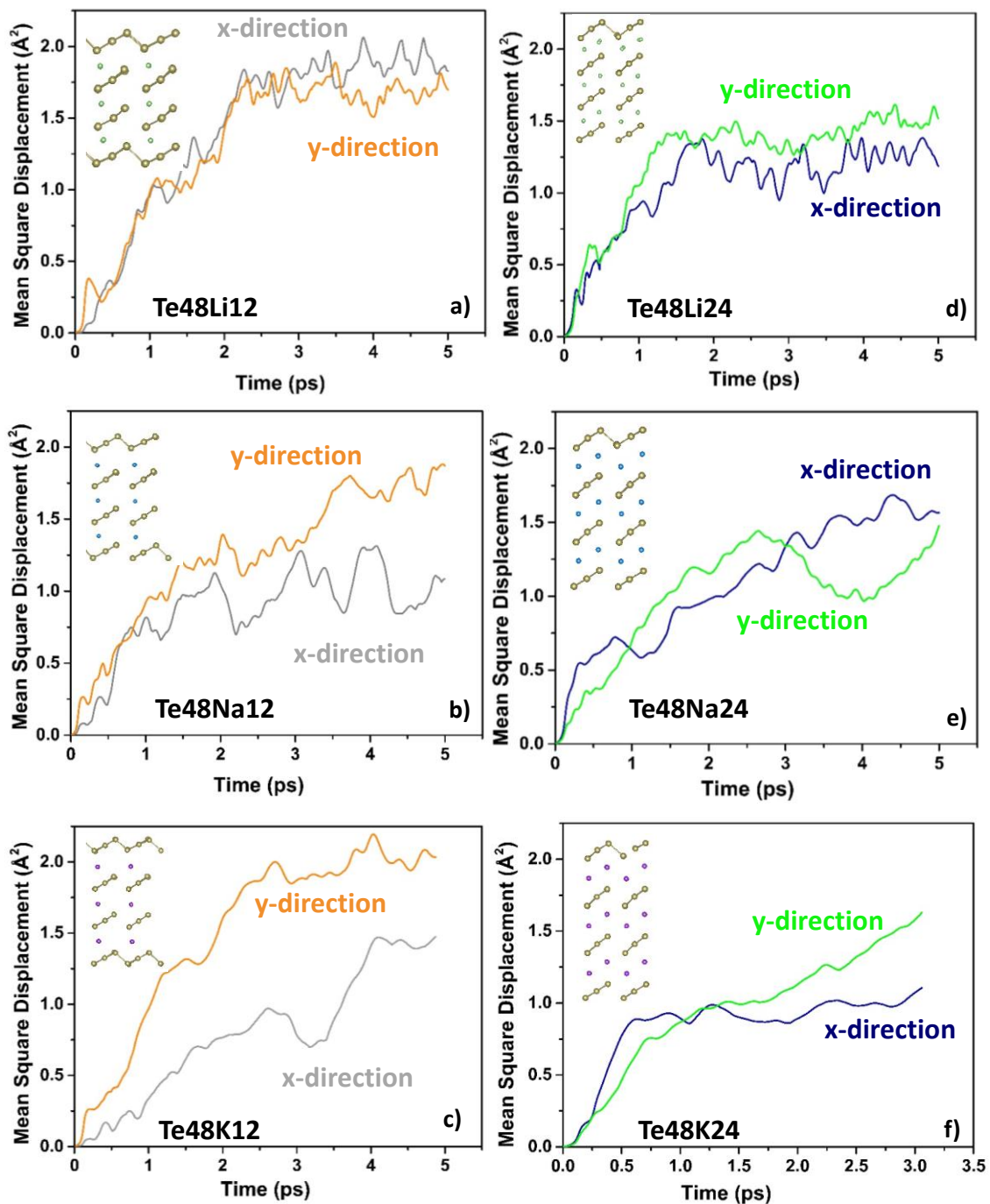


Figure 3 | Mean square displacement of alkali ions calculated by using ab-initio MD. (a-f) Mean square displacement of (a & d) Li, (b & e) Na, and (c & f) K in (a-c) $\text{Te}_{48}\text{A}_{12}$ and (d-f) $\text{Te}_{48}\text{A}_{24}$ configurations. A denotes an alkali atom (i.e., Li, Na, or K).

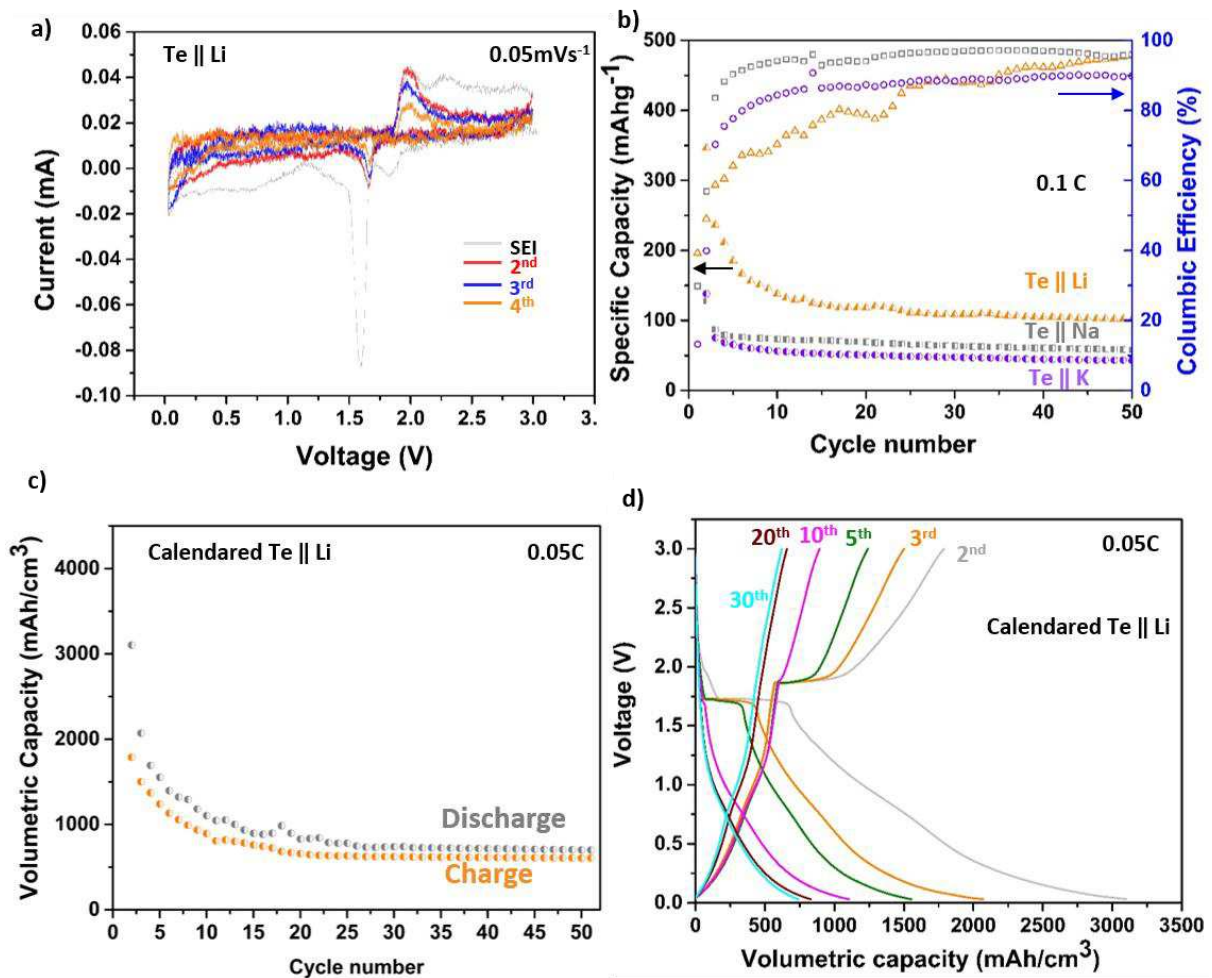


Figure 4 | Performance of Te||Li, Te||Na, and Te||K half-cell batteries. (a) CV testing of Te||Li at scanning rate of $\sim 0.05 \text{ mVs}^{-1}$. (b) Gravimetric performance and columbic efficiency of Te||Li, Te||Na, and Te||K batteries at current density of $\sim 0.1 \text{ C}$. (c) Volumetric performance of calendared Te||Li at a current density of $\sim 0.05 \text{ C}$. (d) Electrochemical charge and discharge voltage profile of the calendared Te||Li battery at a current density of $\sim 0.05 \text{ C}$. ($1 \text{ C} = 100 \text{ mAh}^{-1}$).

Figures

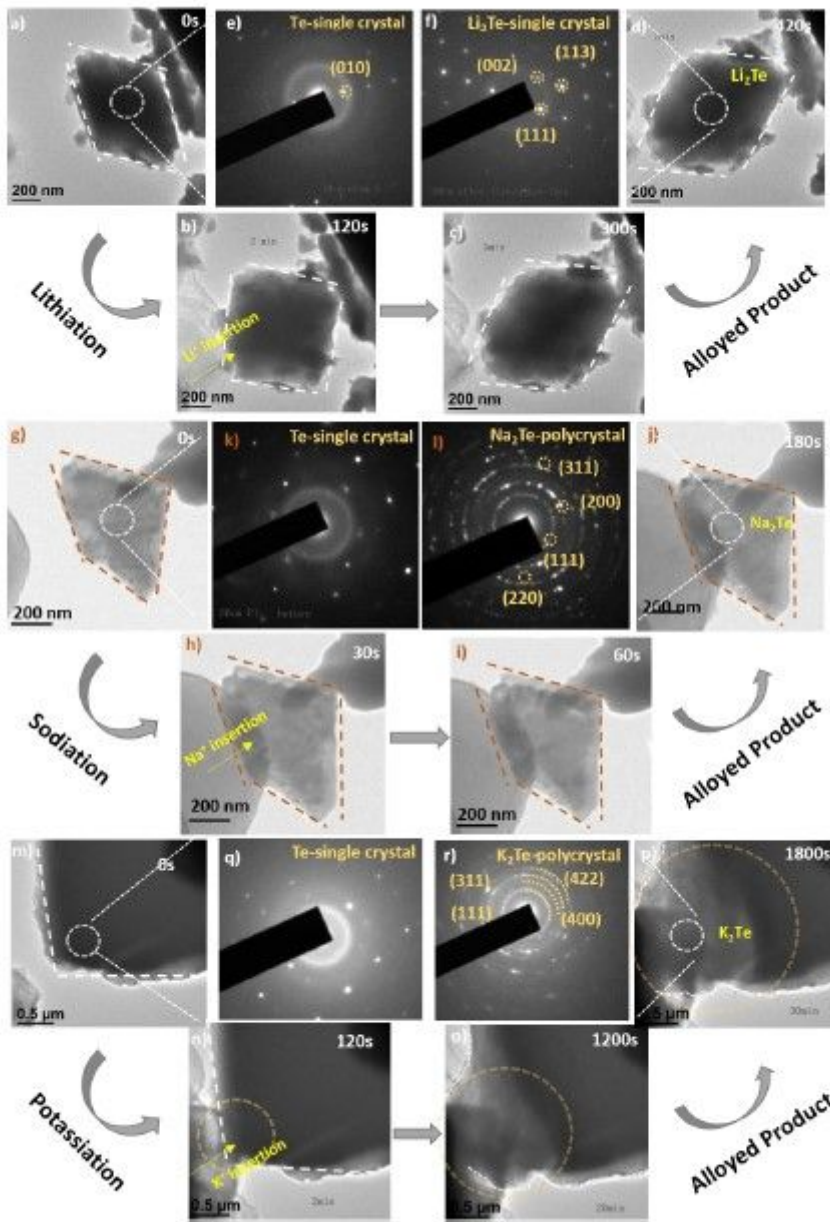


Figure 1

In-situ TEM study of alkali ion insertion in Te. TEM images of Te (a) before (0s) and after (b) 120 s, (c) 300 s, and (d) complete (420s) lithium ion insertion. Corresponding SAED patterns of (e) pristine Te and (f) lithiated Te. TEM images of Te (g) before (0s) and after (h) 30 s, (i) 60 s and (j) complete (180 s) sodium ion insertion. Corresponding SAED patterns of (k) pristine Te and (l) sodiated Te. TEM images of Te (m) before (0s) and after (n) 120 s, (o) 1200 s and (p) complete (1800 s) potassium ion insertion. Corresponding SAED patterns of (q) pristine Te and (r) potassiated Te.

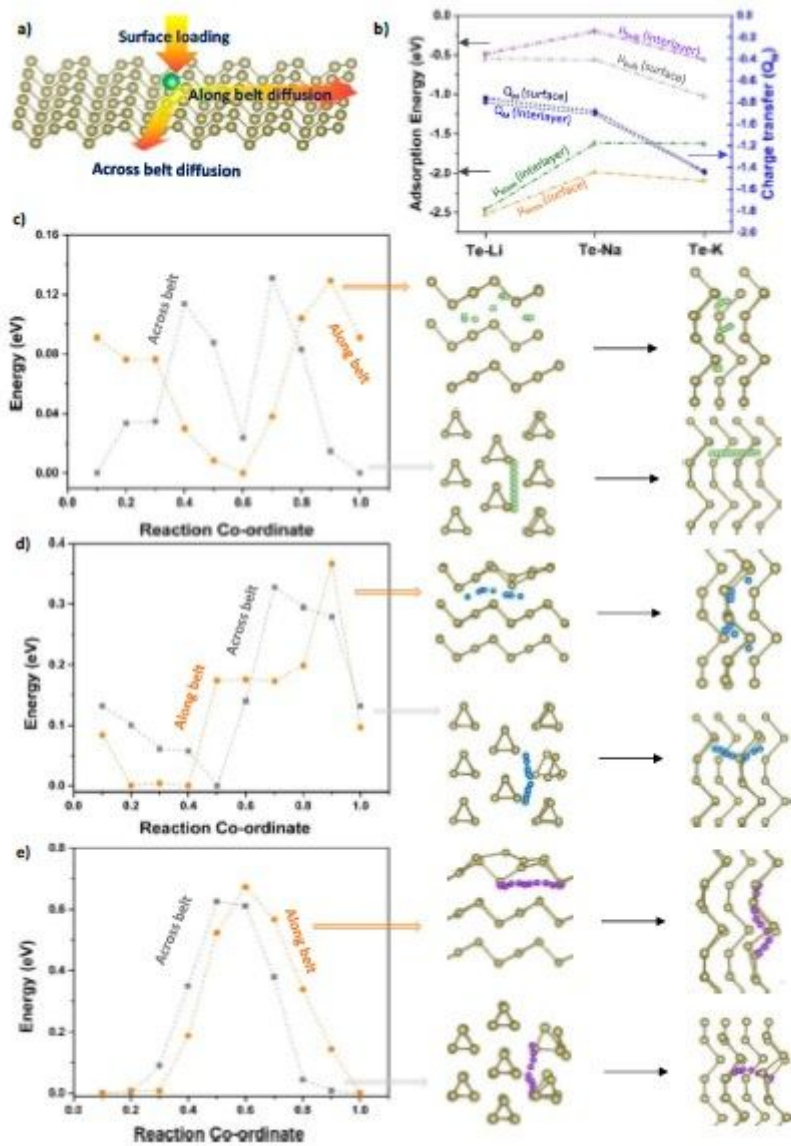


Figure 2

DFT study of interaction between Te and alkali ions. (a) Schematic illustration of alkali atom adsorption and diffusion through the "along-belt" and "across-belt" directions. (b) Adsorption energy of different alkali atoms on the surface and in the interior of Te, calculated using μ_{atom} and μ_{bulk} method and charge transfer between alkali ions and Te sheets. (c-e) Diffusion energy barrier "along-belt" and "across-belt" for (c) Li, (d) Na, and (e) K migration in interior of few-layered Te. Corresponding simulated structures are also shown.

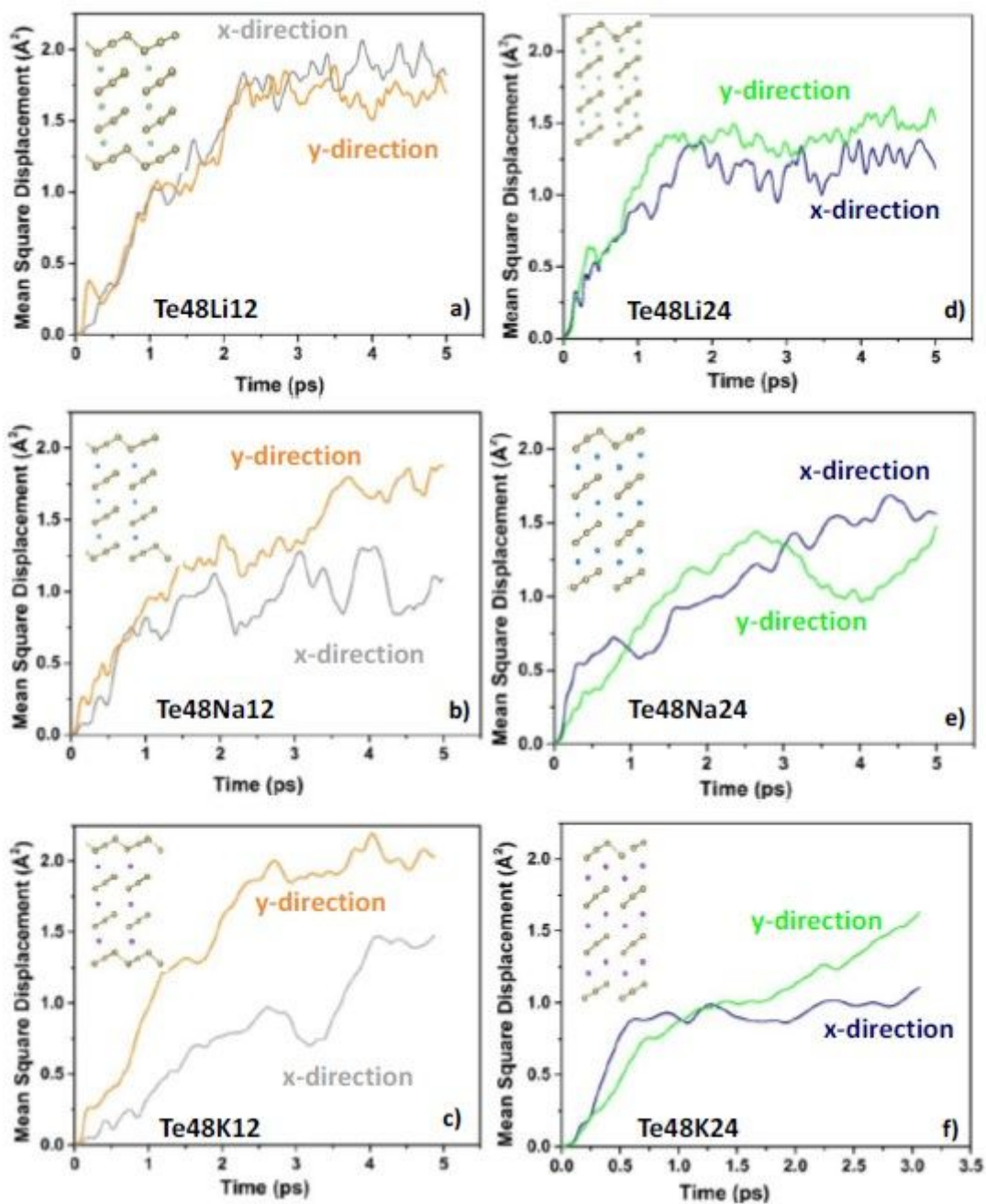


Figure 3

Mean square displacement of alkali ions calculated by using ab-initio MD. (a-f) Mean square displacement of (a & d) Li, (b & e) Na, and (c & f) K in (a-c) Te48A12 and (d-f) Te48A24 configurations. A denotes an alkali atom (i.e., Li, Na, or K).

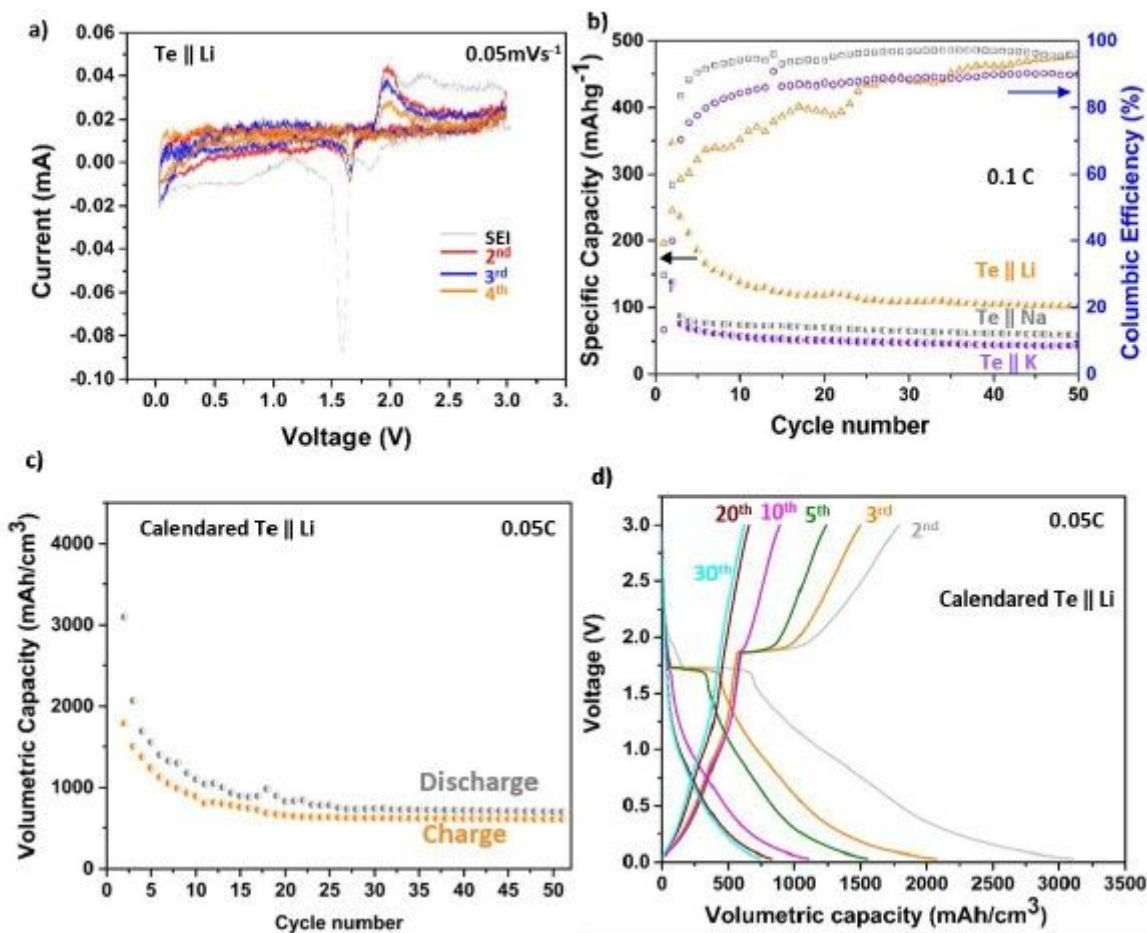


Figure 4

Performance of Te||Li, Te||Na, and Te||K half-cell batteries. (a) CV testing of Te||Li at scanning rate of $\sim 0.05 \text{ mVs}^{-1}$. (b) Gravimetric performance and columbic efficiency of Te||Li, Te||Na, and Te||K batteries at current density of $\sim 0.1 \text{ C}$. (c) Volumetric performance of calendared Te||Li at a current density of $\sim 0.05 \text{ C}$. (d) Electrochemical charge and discharge voltage profile of the calendared Te||Li battery at a current density of $\sim 0.05 \text{ C}$. ($1 \text{ C} = 100 \text{ mAh}^{-1}$).

Supplementary Files

This is a list of supplementary files associated with this preprint. Click to download.

- [Sl.pdf](#)